Published in final edited form as:

Mol Imaging Biol. 2020 August ; 22(4): 1003–1011. doi:10.1007/s11307-020-01478-9.

Assessment of Metastatic and Reactive Sentinel Lymph Nodes with B7-H3-Targeted Ultrasound Molecular Imaging: A Longitudinal Study in Mouse Models

Fengyang Zheng[1,2,3,$], **Pan Li**[1,4,5,$], **Sunitha V. Bachawal**[1], **Huaijun Wang**[1], **Chaolun Li**[2,3], **Wei Yuan**[6], **Beijian Huang**[2,3,*], **Ramasamy Paulmurugan**[1,*]

[1]Department of Radiology, Molecular Imaging Program at Stanford (MIPS), Stanford University School of Medicine, 3155 Porter Drive, Palo Alto, CA 94305, USA

[2]Department of Ultrasound, Zhongshan Hospital, Fudan University, 180 Fenglin Rd, Shanghai 200032, P.R. China

[3]Shanghai Institute of Medical Imaging, Shanghai 200032, P.R. China

[4]Institute of Ultrasound Imaging of Chongqing Medical University, Chongqing 400010, P.R. China

[5]Department of Ultrasound, The Second Affiliated Hospital of Chongqing Medical University, Chongqing, 400010, P.R. China

[6]Department of pathology, Zhongshan Hospital, Fudan University, 180 Fenglin Rd, Shanghai 200032, P.R. China

Abstract

Purpose: To explore the potential of B7-H3-targeted ultrasound molecular imaging (USMI) for longitudinal assessment and differentiation of metastatic and reactive sentinel lymph nodes (SLNs) in mouse models.

Procedures: Metastatic and reactive SLN models were established by injection of 4T1 breast cancer cells and Complete Freund's Adjuvant (CFA) respectively to the 4th mammary fat pad of female BALB/c mice. At day 21, 28, and 35 after inoculation, USMI was performed following intravenous injection of B7-H3-targeted microbubbles ($MB_{B7\text{-}H3}$) or IgG-control microbubbles ($MB_{control}$). All SLNs were histopathologically examined after the last imaging session.

Results: A total of 20 SLNs from tumor-bearing mice (T-SLNs) and five SLNs from CFA-injected mice (C-SLNs) were examined by USMI. Nine T-SLNs were histopathologically positive for metastasis (MT-SLNs). From day 21 to 35, T-SLNs showed a rising trend in $MB_{B7\text{-}H3}$ signal

---

Corresponding authors: 1. Ramasamy Paulmurugan, PhD, Molecular Imaging Program at Stanford (MIPS), Stanford University School of Medicine, 3155 Porter Drive, Palo Alto, CA 94304, USA., Fax: 650-721-6921;, paulmur8@stanford.edu, 2. Beijian Huang, MD&PhD, Department of ultrasound, Zhongshan Hospital, Fudan University, Shanghai Institute of Medical Imaging, 180 Fenglin Rd, Shanghai 200032, P.R. China., Fax: 64220319, huang.beijian@zs-hospital.sh.cn.

[$]Fengyang Zheng and Pan Li contributed equally to this work

[*]Ramasamy Paulmurugan and Beijian Huang contributed equally to this work

Conflict of Interests

The authors declare that they have no conflict of interest related to this study.

Ethical approval

All applicable institutional and/or national guidelines for the care and use of animals were followed.

with a steep increase in MT-SLNs at day 35 (213.5 ± 80.8 a.u.) as compared to day 28 (87.6 ± 77.2 a.u., $P=0.002$) and day 21 (55.7 ± 35.5 a.u., $P<0.001$). At day 35, MT-SLNs had significantly higher $MB_{B7\text{-}H3}$ signal than non-metastatic T-SLNs (NMT-SLNs) (101.9 ± 48.0 a.u., $P=0.001$) and C-SLNs (38.5 ± 34.0 a.u., $P=0.001$); $MB_{B7\text{-}H3}$ signal was significantly higher than $MB_{control}$ in MT-SLNs ($P=0.001$), but not in NMT-SLNs or C-SLNs (both $P>0.05$). A significant correlation was detected between $MB_{B7\text{-}H3}$ signal and volume fraction of metastasis in MT-SLNs (r=0.76, $P=0.017$).

Conclusions: B7-H3-targeted USMI allows differentiation of MT-SLNs from NMT-SLNs and C-SLNs in mouse models and has great potential to evaluate tumor burden in SLNs of breast cancer.

Keywords

Ultrasound imaging; Molecular imaging; Sentinel lymph node; Metastasis

Introduction

Determination of axillary lymph node (ALN) status is critical for tumor staging, prognostication, and guidance for treatment in breast cancer patients [1–4]. ALN dissection is a reliable means to identify nodal metastasis but carries a significant risk of complications such as lymphedema, paresthesia, seroma, and limited shoulder motion [5, 6]. As a less morbid procedure, sentinel lymph node dissection (SLND) has replaced ALN dissection as the current reference-standard test for nodal staging in breast cancer with clinical node-negative patients [6, 7]. Nonetheless, SLND remains a surgical procedure performed under general anesthesia, with a considerable proportion of patients (7–41%) suffering postoperative complications [6, 8]. SLND is reliant upon two tracers to locate sentinel lymph nodes (SLNs), an expensive radioactive isotope and a blue dye that may cause severe anaphylaxis [9]. Even with the combination of two tracers, SLND fails to identify axillary malignancies in breast cancer patients with false-negative rates ranging from 5.1% to 9.4% [10]. In addition, the majority of patients (74%) who undergo SLND are pathologically negative [11]. Therefore, a noninvasive method for a more accurate assessment of SLN status is warranted.

Ultrasound (US) is a portable, noninvasive, and relatively inexpensive imaging modality and has been widely used to evaluate ALN status in breast cancer patients [12]. Using conventional US, metastatic lymph nodes commonly appear with cortical thickening, a round shape, absence of an echogenic hilum, and peripheral or mixed vascularity in Doppler imaging mode [12, 13]. However, the diagnostic capability of conventional US for nodal metastasis is not satisfactory [12, 14]; early or small metastases without obvious morphologic changes might be misdiagnosed, necessitating a more reliable and sensitive imaging technique with a higher diagnostic accuracy [15]. Contrast-enhanced ultrasound imaging (CEUS) following subdermal or peritumoral injection of contrast agents (microbubbles) has been developed to detect and depict SLNs in both clinical and preclinical animal studies. The accuracy of SLN detection by CEUS is high [16–18], but the diagnostic accuracy, especially specificity, of CEUS for SLN status is rather limited [16, 17, 19]. CEUS following intravenous administration of microbubbles was also used for lymph node characterization with advantages of getting access to the lymph node directly through nodal blood supply and enabling the simultaneous evaluation of both primary tumors and lymph nodes. However, the performance of this strategy is inconsistent between previous studies and seems not to contribute to a higher diagnostic accuracy for lymph node metastasis [20–23].

Ultrasound molecular imaging (USMI) is a novel imaging approach with high potential to better characterize tumors, and thus improve diagnostic accuracy of conventional US [24]. Using molecularly-targeted contrast microbubbles, USMI has the advantages of both US and molecular imaging and has been recently translated to first in-human clinical trials in cancer imaging [25]. Targeted contrast agents are created by conjugating target specific binding ligands to the microbubble shell to make them firmly attach to the molecular targets of tumor vasculature [26]. B7-H3, also known as CD276, was discovered recently as a novel tumor neovasculature associated marker that is differentially expressed in several cancer types such as colon, breast, lung, etc. [27]. Previous studies have confirmed high protein expression of B7-H3 in both tumor cells and tumor neovasculature with murine and human breast cancer tissues [28–30]. In breast cancer patients, tumor expression of B7-H3 was suggested as a predictor of early regional lymph node metastasis [30, 31]. B7-H3 expression was also detected in metastatic lymph nodes from breast cancer patients [30], suggesting it as a promising molecular imaging target for metastatic SLNs. B7-H3-targeted microbubbles ($MB_{B7\text{-}H3}$) were previously shown to differentiate breast cancer from benign entities in a transgenic mouse model with a high diagnostic accuracy [28].

To the best of our knowledge, the application of USMI to metastatic SLN depiction has been limited [32], and $MB_{B7\text{-}H3}$ have never been used for characterizing SLNs. Physiologically, lymph nodes are constantly exposed to varying levels of different types of antigens and thus show varying degrees of reactive changes [33]. Enlarged reactive lymph nodes frequently exist along the lymphatic drainage pathways, particularly of large and/or necrotic tumors, which may mimic metastatic lymph nodes [34]. The aim of this study is to assess the feasibility of USMI with $MB_{B7\text{-}H3}$ to longitudinally evaluate and differentiate metastatic SLNs from reactive SLNs in mouse models of orthotopic breast cancer and Complete Freund’s Adjuvant (CFA) mediated inflammation.

Materials and methods

Fig. 1 schematically summarizes the overall study design.

Cell culture and animal models

4T1 murine breast cancer cells were used for creating syngeneic orthotopic tumor models in immunocompetent BALB/c mice. All animal procedures were approved by the Institutional Administrative Panel on Laboratory Animal Care. The metastatic SLN model (n=21) was developed by injecting 1×10^6 4T1 cells to the right 4^{th} mammary fat pad of BALB/c mice. Similarly, the reactive SLN model (n=6) was established by administration of 40 µl of complete Freund’s adjuvant (CFA) (Sigma-Aldrich) to the same location in another group of BALB/c mice to produce local inflammation. At day 10 after 4T1 cell implantation or CFA injection, the SLNs of the animal models were located by peri-inflammation and peritumoral injection of 25 µl of 0.4% Trypan blue solution (Thermo Scientific) in a CFA-injected mouse and a 4T1 tumor-bearing mouse, respectively, and both mice were euthanized and dissected to locate the SLNs. At day 22 to 23 after 4T1 cell implantation, primary tumors were surgically removed under a strict aseptic operation procedure to extend the survival of the tumor-bearing mice [35, 36]. The SLNs were located by peri-inflammation and peritumoral injection of 25 µl of 0.4% Trypan blue solution (Thermo Scientific). The size of SLNs from tumor-bearing mice (T-SLNs, n=20) and CFA-injected mice (C-SLNs, n=5) was monitored by B-mode US imaging at day 0 (baseline), 7, 14, 21, 28, and 35 post-injection of 4T1 cells or CFA. For additional details please refer to Supplementary Methods.

Microbubble characterization

Preclinical streptavidin-coated microbubbles (VisualSonics) were incubated with biotinylated rat anti-mouse B7-H3 antibody (eBioscience) to generate B7-H3-targeted microbubbles ($MB_{B7\text{-}H3}$). As a control group, IgG-control microbubbles ($MB_{control}$) were generated by using biotinylated isotype-matched control immunoglobulin G (IgG) (eBioscience) with the same incubation method. The integrity of the microbubbles was characterized before and after incubation with rat anti-mouse B7-H3 antibody or isotype-matched IgG antibody using Coulter counter (AccuComp Z2; Beckman Coulter Life Sciences). The functional conjugation efficiency of rat anti-mouse B7-H3 antibody to the microbubbles was evaluated using fluorescence activated cell sorter (FACS) analysis. Additional details are included in the Supplementary Methods.

USMI and image analysis

USMI was performed at day 21, 28, and 35 for all the SLNs (n=25) following intravenous administration of 5×10^7 $MB_{B7\text{-}H3}$ or $MB_{control}$ (in random order) on the largest cross section of SLNs using a dedicated small-animal high resolution US imaging system (Vevo 2100, VisualSonics). Four minutes after administration, a continuous high-power destructive pulse (3.7 MPa; transmit power, 100%; mechanical index, 0.63) was applied to destroy all microbubbles within the imaging plane. Imaging data sets were analyzed offline in random order using a commercially available software (Vevo CQ, VisualSonics). The magnitude of imaging signal (expressed in arbitrary units, a.u.) from bound microbubbles were assessed by subtracting the average post-destruction signal from the average pre-destruction signal as described previously [37]. A detailed description of USMI protocol is provided in the Supplementary Methods.

Ex vivo tissue analysis

After the last imaging session (day 35), *ex vivo* hematoxylin and eosin (H&E, Scytek) staining and immunofluorescence using rat anti-mouse B7-H3 antibodies (eBiosciences) were performed for all examined SLNs (n=25) and primary tumors (n=20) using standard techniques (See Supplementary Methods). For T-SLNs presenting metastases, volume fraction of metastasis (VFM) was calculated as shown in the Supplementary figure 1.

Immunofluorescence staining

Paraffin-embedded primary tumor sections (n=20) and MT-SLN sections (n=9) with the largest area of metastasis (confirmed by their adjacent H&E-stained sections) were selected to proceed with immunofluorescence staining. After deparaffinization and rehydration, tissue sections were placed in pre-warmed (94–96°C) sodium citrate buffer (pH 6.0, Abcam) maintained at a sub-boiling temperature for 10 minutes to unmask antigens; this is followed by cooling down at room temperature for 30 minutes and subsequent blocking with 3% bovine serum albumin solution (Sigma-Aldrich) containing 3% donkey serum and 3% goat serum for 1 hour at room temperature. Sections were then co-incubated with rat anti-mouse B7-H3 (eBiosciences) and rabbit anti-mouse CD31 (Abcam) antibodies overnight at 4°C at a dilution of 1:50 and 1:100, respectively. Above primary antibodies were visualized by using AlexaFluor-488 conjugated donkey anti-rat or AlexaFluor-546 conjugated goat anti-rabbit secondary antibodies, respectively (Invitrogen). The fluorescent sections were imaged using a digital slide scanner (Nanozoomer; Hamamatsu) with exposure time of 3 seconds for both FITC and Trtc channels.

Statistical analysis

All data were expressed as the means ± standard deviation. For SLN size and USMI, data sets with equal variances were compared by one-way ANOVA followed by a Bonferroni’s multiple comparisons test; data sets with unequal variances were compared by a Tamhane’s T2 test. The correlation between VFM and $MB_{B7\text{-}H3}$ signal was analyzed by Pearson correlation analysis. The performance of B7-H3-targeted molecular imaging in differentiating metastatic and non-metastatic SLNs was evaluated using receiver-operating characteristic (ROC) analysis and the area under the curve (AUC). SPSS 21.0 software (IBM Corporation) was used for data analysis. A P value of less than 0.05 was accepted as statistically significant.

Results

Establishment of metastatic and reactive SLNs

Immediately after the injection of Trypan blue solution, a blue-labeled lymphatic vessel deriving from the injecting site was observed towards the ipsilateral inguinal lymph node which is also slightly labeled by the blue dye several seconds later (Fig. 2a–b). The blue-labeled inguinal lymph node was further confirmed after removal of the skin and thus was determined as the SLNs in our experimental animal models. Fig. 2c summarizes the size measurement of T-SLNs and C-SLNs from day 0 to day 35. T-SLN size increased over time, followed by a slight drop at day 21; a dramatic size increase in T-SLNs was observed at day 35 as compared to day 21 (P=0.005). A progressive size increase in C-SLNs was observed from day 0 to day 21, which was followed by a gradual decrease up to day 35.

By H&E histological analysis, 9 out of 20 T-SLNs showed the presence of metastasis and were defined as metastatic T-SLNs (MT-SLNs), while the other 11 T-SLNs without metastasis were defined as non-metastatic T-SLNs (NMT-SLNs).

Microbubble characterization

We evaluated streptavidin coated microbubbles for their size and distribution before and after functionalizing with B7-H3 or iso-IgG antibodies using Coulter counter and FACS analysis. Similarly, B7-H3 conjugation efficiency was evaluated by FACS analysis. The results showed no significant variation in the microbubble size before and after functionalization with B7-H3 or iso-IgG antibodies (Supplementary Fig. 2). Similarly, FACS analysis showed efficient conjugation of B7-H3 antibody to the microbubbles (Supplementary Fig. 3).

Longitudinal assessment of B7-H3-targeted USMI in MT-SLNs, NMT-SLNs and C-SLNs

Fig. 3 reveals longitudinal assessment of USMI signal from $MB_{B7\text{-}H3}$ and $MB_{control}$ in C-SLNs, NMT-SLNs, and MT-SLNs, respectively. From day 21 to 35, NMT-SLNs and MT-SLNs showed a rising trend in both $MB_{B7\text{-}H3}$ signal and $MB_{control}$ signal, with a steep increase of $MB_{B7\text{-}H3}$ signal in MT-SLNs at day 35 (213.5 ± 80.8 a.u.) as compared to day 28 (87.6 ± 77.2 a.u., P=0.002) and day 21 (55.7 ± 35.5 a.u., P<0.001), while C-SLNs showed a declining trend in both $MB_{B7\text{-}H3}$ signal and $MB_{control}$ signal. At day 35, MT-SLNs presented significantly higher $MB_{B7\text{-}H3}$ signal than NMT-SLNs (101.9 ± 48.0 a.u., P=0.001) and C-SLNs (38.5 ± 34.0 a.u., P<0.001), while such difference was not observed in $MB_{control}$ signal (all P>0.05); MT-SLNs showed significantly higher $MB_{B7\text{-}H3}$ signal than $MB_{control}$ signal (213.5 ± 80.8 a.u. vs 98.0 ± 35.2 a.u., P=0.001), while no significant difference was detected between $MB_{B7\text{-}H3}$ signal and $MB_{control}$ signal in NMT-SLNs or C-SLNs (both P>0.05). Comparison between $MB_{B7\text{-}H3}$ and $MB_{control}$ signal in MT-SLNs, NMT-SLNs, and C-SLNs is shown in Supplementary figure 4. ROC analysis showed that AUC of $MB_{B7\text{-}H3}$ signal for differentiating MT-SLNs from NMT-SLNs and C-SLNs was 0.91 (95% confidence interval (CI): 0.77, 1.00) (Supplementary Fig. 5).

Ex vivo analysis

Different proliferative alterations were observed in C-SLNs, NMT-SLNs and normal lymphatic tissues of MT-SLNs (Supplementary Fig. 6). B7-H3 expression was observed both on the tumor neovasculature and on tumor epithelial cells in primary tumors and MT-SLNs (Supplementary Fig. 7).

Correlation of B7-H3-targeted imaging signal with VFM in MT-SLNs

A wide variation of $MB_{B7\text{-}H3}$ signal in MT-SLNs, ranging from 48.8 a.u. to 311.8 a.u., prompted the hypothesis that $MB_{B7\text{-}H3}$ signal may correlate with VFM in MT-SLNs. As expected, VFM in the nine MT-SLNs ranged from 8% to 86%, and a significant correlation was detected between $MB_{B7\text{-}H3}$ signal and VFM (Pearson correlation coefficient (r): 0.76; 95% CI: 0.59, 0.94; P=0.017) (Supplementary Fig. 8). Representative H&E-stained sections with low and high VFM along with corresponding US images, including a color map representing $MB_{B7\text{-}H3}$ signal, are shown in Fig. 4 and Fig. 5, respectively. The scale for the color maps was kept constant for all images.

Discussion

In this study, we established metastatic and reactive SLN mouse models and showed that USMI using $MB_{B7\text{-}H3}$ allows longitudinal assessment and differentiation of metastatic and reactive SLNs. A previous study has shown that USMI using dual-targeted microbubbles (P-selectin and $\alpha_v\beta_3$-integrin) can aid in detecting metastatic SLNs in melanoma [32]. However, P-selectin expression levels change after an inflammatory stimulus [38] and $\alpha_v\beta_3$-integrin has been shown to express in granuloma [39]. Therefore, targeted microbubbles with a higher specificity for the detection of metastatic lymph nodes are warranted. Since enlarged reactive lymph nodes are frequently present along the lymphatic drainage pathways of tumors and can mimic lymph node metastasis [34], it is important to evaluate whether USMI allows differentiation of enlarged reactive nodes from metastatic nodes. To the best of our knowledge, this study is the first that have attempted to perform SLN characterization using B7-H3-targeted USMI in metastatic and reactive SLNs in mouse models.

We employed a syngeneic metastatic 4T1 triple negative breast tumor model in immunocompetent BALB/c mice which provided a tumor microenvironment with compatible stromal, vascular, and immunologic milieu [40]. This syngeneic breast cancer model spontaneously develops metastases in SLNs that mimics human breast cancer patients [35, 41]. One limitation of this model is the fast growth rate of tumors [35] that may grow to the size limit allowed by the Animal Research Compliance regulation before metastases can be detected in SLNs. Hence, we surgically removed the primary tumor when it reached a certain size range ($308.4 \pm 57.8\ mm^3$) to extend the life span of the tumor-bearing mice and allow tumor to metastasize to SLNs [35]. Localized inoculation of CFA enhances antibody production and induces an inflammatory response at the injection site [42], which was used as reactive SLN model in this study. Consistent with previous studies [42, 43], both T-SLNs and C-SLNs showed size enlargement at early time points, which may be due to a direct innate immune reaction [44] and/or a primary immune response to antigens from tumor or CFA being presented by antigen-presenting cells [45]. From day 21 to 35, T-SLNs presented a dramatic size enlargement while C-SLNs showed a declining trend of size development, which is similar to the results of an earlier study where they used rabbit model for the study [45].

In our longitudinal assessment of USMI, T-SLNs showed a rising trend in both $MB_{B7\text{-}H3}$ signal and $MB_{control}$ signal, while C-SLNs showed a declining trend, corresponding to their size changes from day 21 to 35. Since vascular status is an important factor that influences the binding of microbubbles to molecular targets expressed on endothelial cells [46], varied hypervascular responses of T-SLNs and C-SLNs to tumor and inflammation progress may account for their different signal patterns over time [45]. Further studies are needed to explore the relationship between USMI and vascular status to improve the diagnostic performance of USMI. Although unavoidable responses of SLNs to external stimuli could potentially complicate a vascular-targeted imaging approach, B7-H3-targeted USMI was shown to be capable of differentiating MT-SLNs from NMT-SLNs and C-SLNs with great efficiency in our mouse models.

B7-H3 is a member of the B7 family of immunoregulators that is expressed at low levels in most normal tissues but is overexpressed in a broad spectrum of cancers including tumor vasculatures [27, 47]. Although the underlying mechanism of its function in cancer has remained unclear, B7-H3 was identified as a predictor of poor prognosis and increased risks for metastasis [47]. B7-H3 overexpression is highly prevalent in various breast cancer cell lines and breast tumors of both murine and human, and is associated with positive lymph node metastasis [30, 31, 48]. Coincidently, our study detected B7-H3 expression both on the tumor neovasculature and on tumor epithelial cells not only in primary tumors but also in MT-SLNs. In support of our results, B7-H3 protein was also reported to express in all metastatic lymph nodes from breast cancer patients [30], suggesting it as a promising molecular target for detecting lymph node metastasis. This is further supported by our results that at day 35, MT-SLNs had significantly higher $MB_{B7\text{-}H3}$ signal than NMT-SLNs and C-SLNs. In addition, $MB_{B7\text{-}H3}$ signal was much higher than $MB_{control}$ signal in MT-SLNs, but not in NMT-SLNs or C-SLNs. Our results confirmed the hypothesis that B7-H3 has great potential as a molecular target for nodal characterization in breast cancer.

Notably, Pearson correlation analysis revealed a significant correlation (r=0.76) between $MB_{B7\text{-}H3}$ signal and VFM in MT-SLNs. A previous study also noted that signal from dual-targeted microbubbles were different among metastatic lymph nodes, which might be caused by varied metastatic stages of lymph nodes among their animal models [32]. In addition, an earlier study proved that $MB_{B7\text{-}H3}$ signal correlated well (r=0.77) with B7-H3 expression in a transgenic mouse model of breast cancer. These results indicate that the extent of metastasis, partially equivalent to the number of molecular targets in SLNs affects USMI signal. In this study we observed that $MB_{B7\text{-}H3}$ were not able to detect early metastases in SLNs due to overlaps between $MB_{B7\text{-}H3}$ signal in MT-SLNs with low VFM and NMT-SLNs/C-SLNs. Considering the fact that ALN dissection is not recommended for women with early-stage breast cancer and limited SLN metastasis based on the American College of Surgeons Oncology Group Z0011 trial [49], noninvasive differentiation of SLN tumor burden in the diagnostic period remains clinically important, which would aid surgical decision making. In addition, B7-H3 has emerged as a new potential therapeutic target in several cancer types, and anti-B7-H3 antibodies are currently being studied in several phase I clinical trials [50, 51]. B7-H3-targeted USMI may also be used to evaluate the responses of tumor or metastatic lymph nodes to anti-B7-H3 therapies.

Several limitations existed in our preliminary study. Firstly, the sample size is relatively small, especially for C-LSNs (n=5), which may have limited the statistical significance of the data obtained. Secondly, the imaging plane with the largest SLN cross section was selected subjectively and a single imaging plane might miss small metastases, which would compromise the diagnostic capacity. Three-dimensional USMI would be preferable in future studies. Finally, diagnostic performance of B7-H3-targeted USMI at earlier stages (before day 35) was not evaluated and needs further studies with a larger sample size.

Conclusion

In summary, B7-H3-targeted USMI allows differentiation of metastatic SLNs from non-metastatic and reactive SLNs in mouse models. Moreover, B7-H3-targeted signal correlates well with VFM. Our findings suggest that B7-H3-targeted USMI has great potential to evaluate the presence and extent of metastatic involvement in SLNs, laying the foundation for further studies and clinical translation of this non-invasive imaging approach for SLN characterization.

Supplementary Material

Refer to Web version on PubMed Central for supplementary material.

Acknowledgements

The Canary Center at Stanford, Department of Radiology for facility and resources. We also thank SCi^3 small animal imaging service center, Stanford University School of Medicine for providing imaging facilities and data analysis support. We also acknowledge Dr. José G. Vilches-Moure, Veterinary pathologist, Animal Histology Services (AHS) for his advice regarding histological analysis of tissues.

Funding

This research was partially supported by NIH R01CA209888 (RP), NIH R21EB022298 (RP) and The Teal Foundation.

Abbreviations

ALN	Axillary lymph node
SLN	Sentinel lymph node
SLND	Sentinel lymph node dissection
CEUS	Contrast-enhanced ultrasound imaging
USMI	Ultrasound molecular imaging
CFA	Complete Freund’s adjuvant
$MB_{B7\text{-}H3}$	B7-H3-targeted microbubbles
$MB_{control}$	IgG-control microbubbles
T-SLN	Sentinel lymph nodes from tumor-bearing mice
C-SLN	Sentinel lymph node from CFA-injected mice
MT-SLN	Metastatic sentinel lymph node from tumor-bearing mice
NMT-SLN	Non-metastatic sentinel lymph node from tumor-bearing mice
VFM	Volume fraction of metastasis

Reference

1. Gradishar WJ, Anderson BO, Balassanian R, et al. (2017) NCCN Guidelines Insights: Breast Cancer, Version 1.2017. J Natl Compr Canc Netw 15:433–451. [PubMed: 28404755]
2. Banerjee M, George J, Song EY, et al. (2004) Tree-based model for breast cancer prognostication. J Clin Oncol 22:2567–75. [PubMed: 15226324]

3. Nemoto T, Vana J, Bedwani RN, et al. (1980) Management and survival of female breast cancer: results of a national survey by the American College of Surgeons. Cancer 45:2917–24. [PubMed: 7388735]
4. Fisher B, Bauer M, Wickerham DL, et al. (1983) Relation of number of positive axillary nodes to the prognosis of patients with primary breast cancer. An NSABP update. Cancer 52:1551–7. [PubMed: 6352003]
5. Soares EWS, Nagai HM, Bredt LC, et al. (2014) Morbidity after conventional dissection of axillary lymph nodes in breast cancer patients. World J Surg Oncol 12:67. [PubMed: 24670000]
6. Lucci A, McCall LM, Beitsch PD, et al. (2007) Surgical complications associated with sentinel lymph node dissection (SLND) plus axillary lymph node dissection compared with SLND alone in the American College of Surgeons Oncology Group Trial Z0011. J Clin Oncol 25:3657–63. [PubMed: 17485711]
7. Veronesi U, Paganelli G, Viale G, et al. (2003) A randomized comparison of sentinel-node biopsy with routine axillary dissection in breast cancer. N Engl J Med 349:546–53. [PubMed: 12904519]
8. Ashikaga T, Krag DN, Land SR, et al. (2010) Morbidity results from the NSABP B-32 trial comparing sentinel lymph node dissection versus axillary dissection. J Surg Oncol 102:111–8. [PubMed: 20648579]
9. Montgomery LL, Thorne AC, Van Zee KJ, et al. (2002) Isosulfan blue dye reactions during sentinel lymph node mapping for breast cancer. Anesth Analg 95:385–8, table of contents. [PubMed: 12145056]
10. Pesek S, Ashikaga T, Krag LE, Krag D (2012) The false-negative rate of sentinel node biopsy in patients with breast cancer: a meta-analysis. World J Surg 36:2239–51. [PubMed: 22569745]
11. Krag DN, Anderson SJ, Julian TB, et al. (2007) Technical outcomes of sentinel-lymph-node resection and conventional axillary-lymph-node dissection in patients with clinically node-negative breast cancer: results from the NSABP B-32 randomised phase III trial. Lancet Oncol 8:881–8. [PubMed: 17851130]
12. Esen G, Gurses B, Yilmaz MH, et al. (2005) Gray scale and power Doppler US in the preoperative evaluation of axillary metastases in breast cancer patients with no palpable lymph nodes. Eur Radiol 15:1215–23. [PubMed: 15690206]
13. Esen G (2006) Ultrasound of superficial lymph nodes. Eur J Radiol 58:345–59. [PubMed: 16480846]
14. Alvarez S, Añorbe E, Alcorta P, et al. (2006) Role of sonography in the diagnosis of axillary lymph node metastases in breast cancer: a systematic review. AJR Am J Roentgenol 186:1342–8. [PubMed: 16632729]
15. Mori N, Mugikura S, Miyashita M, et al. (2018) Perfusion contrast-enhanced ultrasound to predict early lymph-node metastasis in breast cancer. Jpn J Radiol.
16. Zhao J, Zhang J, Zhu QL, et al. (2018) The value of contrast-enhanced ultrasound for sentinel lymph node identification and characterisation in pre-operative breast cancer patients: A prospective study. Eur Radiol 28:1654–1661. [PubMed: 29058028]
17. Goldberg BB, Merton DA, Liu J-B, et al. (2004) Sentinel Lymph Nodes in a Swine Model with Melanoma: Contrast-enhanced Lymphatic US. Radiology 230:727–734. [PubMed: 14990839]
18. Wang Y, Cheng Z, Li J, Tang J (2010) Gray-scale contrast-enhanced utrasonography in detecting sentinel lymph nodes: An animal study. Eur J Radiol 74:e55–e59. [PubMed: 19423261]
19. Goldberg BB, Merton DA, Liu J Bin, et al. (2011) Contrast-enhanced ultrasound imaging of sentinel lymph nodes after peritumoral administration of sonazoid in a melanoma tumor animal model. J Ultrasound Med 30:441–453. [PubMed: 21460143]
20. Poanta L, Serban O, Pascu I, et al. (2014) The place of CEUS in distinguishing benign from malignant cervical lymph nodes: a prospective study. Med Ultrason 16:7–14. [PubMed: 24567918]
21. Slaisova R, Benda K, Jarkovsky J, et al. (2013) Contrast-enhanced ultrasonography compared to gray-scale and power doppler in the diagnosis of peripheral lymphadenopathy. Eur J Radiol 82:693–8. [PubMed: 23298797]
22. Hong YR, Luo ZY, Mo GQ, et al. (2017) Role of Contrast-Enhanced Ultrasound in the Pre-operative Diagnosis of Cervical Lymph Node Metastasis in Patients with Papillary Thyroid Carcinoma. Ultrasound Med Biol 43:2567–2575. [PubMed: 28807450]

23. Rubaltelli L, Corradin S, Dorigo A, et al. (2007) Automated quantitative evaluation of lymph node perfusion on contrast-enhanced sonography. Am. J. Roentgenol. 188:977–983. [PubMed: 17377033]
24. Kiessling F, Bzyl J, Fokong S, et al. (2012) Targeted ultrasound imaging of cancer: an emerging technology on its way to clinics. Curr Pharm Des 18:2184–99. [PubMed: 22352772]
25. Abou-Elkacem L, Bachawal SV, Willmann JK (2015) Ultrasound molecular imaging: Moving toward clinical translation. Eur J Radiol 84:1685–93. [PubMed: 25851932]
26. Kiessling F, Fokong S, Bzyl J, et al. (2014) Recent advances in molecular, multimodal and theranostic ultrasound imaging. Adv Drug Deliv Rev 72:15–27. [PubMed: 24316070]
27. Seaman S, Stevens J, Yang MY, et al. (2007) Genes that distinguish physiological and pathological angiogenesis. Cancer Cell 11:539–54. [PubMed: 17560335]
28. Bachawal S V, Jensen KC, Wilson KE, et al. (2015) Breast Cancer Detection by B7-H3-Targeted Ultrasound Molecular Imaging. Cancer Res 75:2501–2509. [PubMed: 25899053]
29. Turtoi A, Dumont B, Greffe Y, et al. (2011) Novel comprehensive approach for accessible biomarker identification and absolute quantification from precious human tissues. J Proteome Res 10:3160–82. [PubMed: 21534635]
30. Arigami T, Narita N, Mizuno R, et al. (2010) B7-H3 ligand expression by primary breast cancer and associated with regional nodal metastasis. Ann Surg 252:1044–1051. [PubMed: 21107115]
31. Liu C, Liu J, Wang J, et al. (2013) B7-H3 expression in ductal and lobular breast cancer and its association with IL-10. Mol Med Rep 7:134–8. [PubMed: 23128494]
32. Nam K, Stanczak M, Forsberg F, et al. (2018) Sentinel Lymph Node Characterization with a Dual-Targeted Molecular Ultrasound Contrast Agent. Mol Imaging Biol 20:221–229. [PubMed: 28762204]
33. Weiss LM, O’Malley D (2013) Benign lymphadenopathies. Mod Pathol 26 Suppl 1:S88–96.
34. Lei J, Xue HD, Li Z, et al. (2010) Possible pathological basis for false diagnoses of lymph nodes by USPIO-enhanced MRI in rabbits. J Magn Reson Imaging 31:1428–1434. [PubMed: 20512896]
35. Paschall A V, Liu K (2016) An Orthotopic Mouse Model of Spontaneous Breast Cancer Metastasis. J Vis Exp 1–7.
36. Tafreshi NK, Enkemann SA, Bui MM, et al. (2011) A mammaglobin-A targeting agent for noninvasive detection of breast cancer metastasis in lymph nodes. Cancer Res 71:1050–9. [PubMed: 21169406]
37. Willmann JK, Paulmurugan R, Chen K, et al. (2008) US imaging of tumor angiogenesis with microbubbles targeted to vascular endothelial growth factor receptor type 2 in mice. Radiology 246:508–18. [PubMed: 18180339]
38. Ley K, Laudanna C, Cybulsky MI, Nourshargh S (2007) Getting to the site of inflammation: the leukocyte adhesion cascade updated. Nat Rev Immunol 7:678–89. [PubMed: 17717539]
39. Jin X, Liang N, Wang M, et al. (2016) Integrin Imaging with 99mTc-3PRGD2 SPECT/CT Shows High Specificity in the Diagnosis of Lymph Node Metastasis from Non-Small Cell Lung Cancer. Radiology 281:958–966. [PubMed: 27479638]
40. Teicher BA (2006) Tumor models for efficacy determination. Mol Cancer Ther 5:2435–43. [PubMed: 17041086]
41. Miller F, Care A (2000) Mouse 4T1 breast tumor model. Curr Protoc Immunol 20:1–16
42. Taub RN, Krantz AR, Dresser DW (1970) The effect of localized injection of adjuvant material on the draining lymph node. I. Histology. Immunology 18:171–86. [PubMed: 4190416]
43. Krzystyniak K, Kozlowska E, Desjardins R, et al. (1995) Different T-cell activation by streptozotocin and Freund’s adjuvant in popliteal lymph node (PLN). Int J Immunopharmacol 17:189–96. [PubMed: 7558513]
44. Jiménez-González M, Plaza-García S, Arizeta J, et al. (2017) A longitudinal MRI study on lymph nodes histiocytosis of a xenograft cancer model. PLoS One 12:1–16.
45. Herman PG, Kim CS, de Sousa MA, Mellins HZ (1976) Microcirculation of the lymph node with metastases. Am J Pathol 85:333–48. [PubMed: 998725]

46. Li C, Torres VC, Tichauer KM (2018) Noninvasive detection of cancer spread to lymph nodes: A review of molecular imaging principles and protocols. J Surg Oncol 118:301–314. [PubMed: 30196532]

47. Li G, Quan Y, Che F, Wang L (2018) B7–H3 in tumors: friend or foe for tumor immunity? Cancer Chemother Pharmacol 81:245–253.

48. Sun J, Guo Y-D, Li X-N, et al. (2014) B7-H3 expression in breast cancer and upregulation of VEGF through gene silence. Onco Targets Ther 7:1979–86. [PubMed: 25378933]

49. Giuliano AE, Ballman KV., McCall L, et al. (2017) Effect of Axillary Dissection vs No Axillary Dissection on 10-Year Overall Survival Among Women With Invasive Breast Cancer and Sentinel Node Metastasis. Jama 318:918. [PubMed: 28898379]

50. Kramer K, Kushner BH, Modak S, et al. (2010) Compartmental intrathecal radioimmunotherapy: results for treatment for metastatic CNS neuroblastoma. J Neurooncol 97:409–18. [PubMed: 19890606]

51. Loos M, Hedderich DM, Friess H, Kleeff J (2010) B7-h3 and its role in antitumor immunity. Clin Dev Immunol 2010:683875. [PubMed: 21127709]

Key Points:

- B7-H3-targeted USMI is a feasible approach to differentiate metastatic SLNs from non-metastatic T-SLNs and reactive SLNs.
- Imaging signal from $\mathrm{MB}_{\mathrm{B7\text{-}H3}}$ was positively correlated with volume fraction of metastasis in MT-SLNs.
- B7-H3-targeted USMI has great potential to evaluate tumor burden in SLNs of breast cancer.

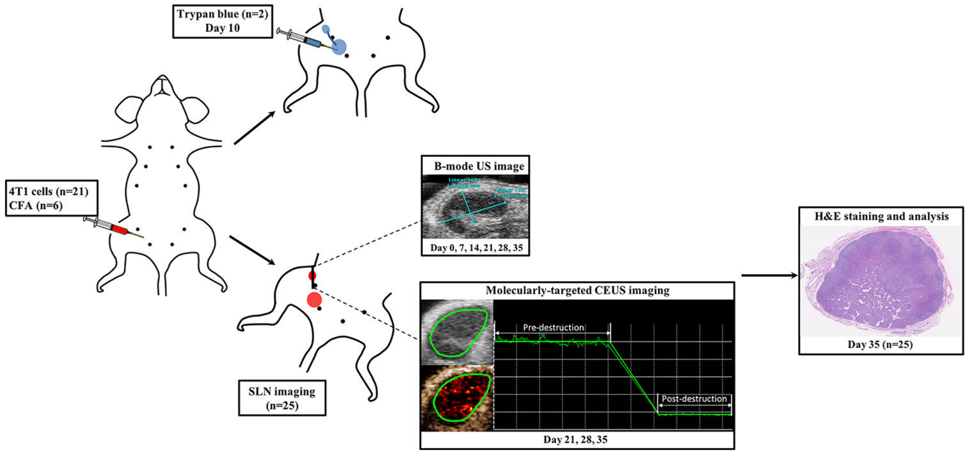

Fig. 1.

Schematic summary of the overall study design. 4T1 tumor-bearing mice (n=21) and CFA-injected mice (n=6) were established. SLNs were detected by peri-inflammation (n=1) and peritumoral (n=1) injection of Trypan blue solution at day 10. The size of T-SLNs (n=20) and C-SLNs (n=5) was monitored by B-mode US imaging at day 0, 7, 14, 21, 28, and 35. Molecularly-targeted CEUS imaging was performed at day 21, 28, and 35 for all the SLNs (n=25) which were histopathologically examined after the last imaging session at day 35.

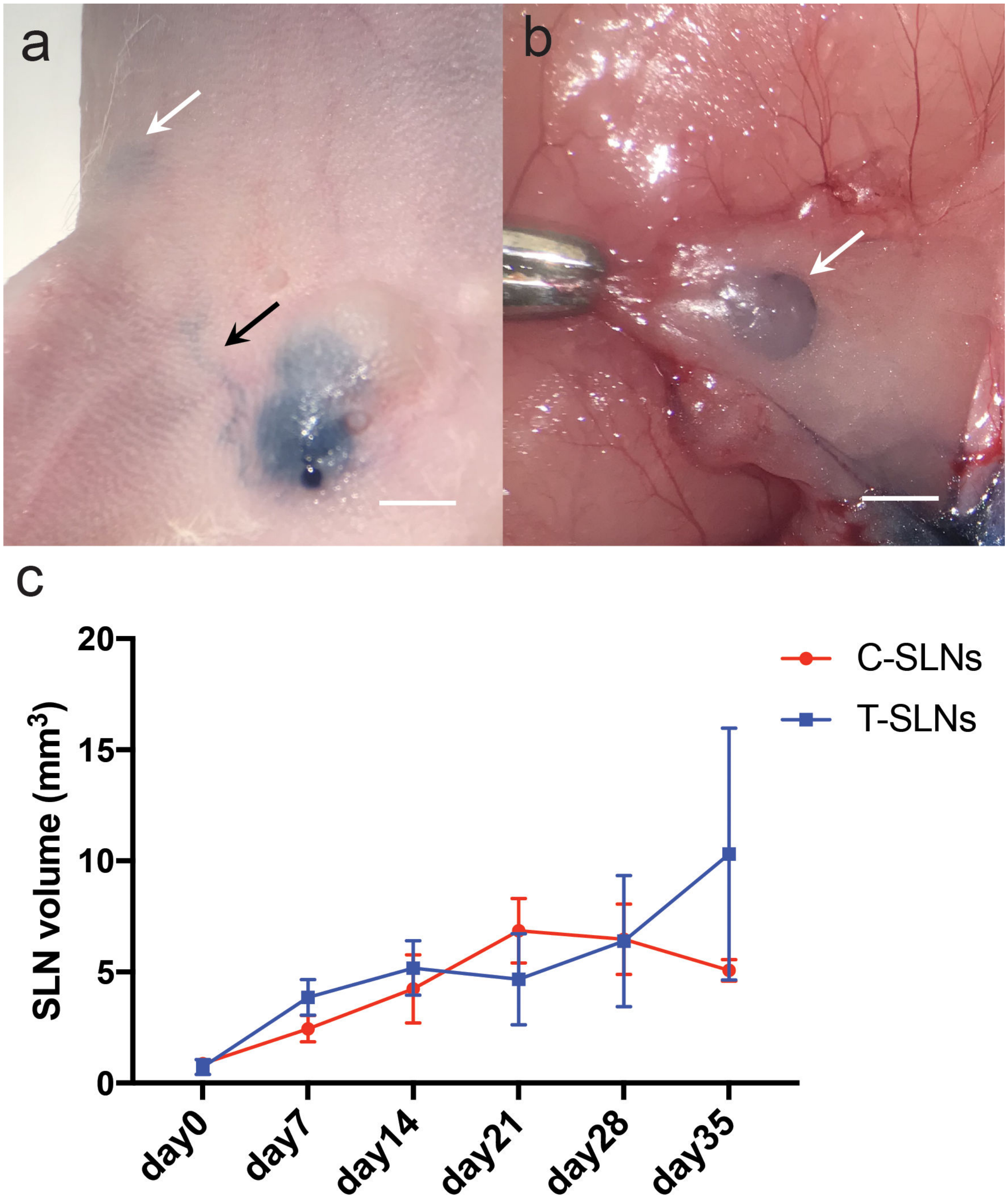

Fig. 2.

SLN detection and size development. (a) a blue-labeled lymphatic vessel (black arrow) was observed connecting the blue-labeled inguinal lymph node (white arrow) and tumor after peritumoral injection of Trypan blue solution; (b) the blue-labeled SLN was detected after the removal of skin. Scare bar=3mm. (c) Size development of T-SLNs and C-SLNs from day 0 to 35 measured by B-mode ultrasound imaging.

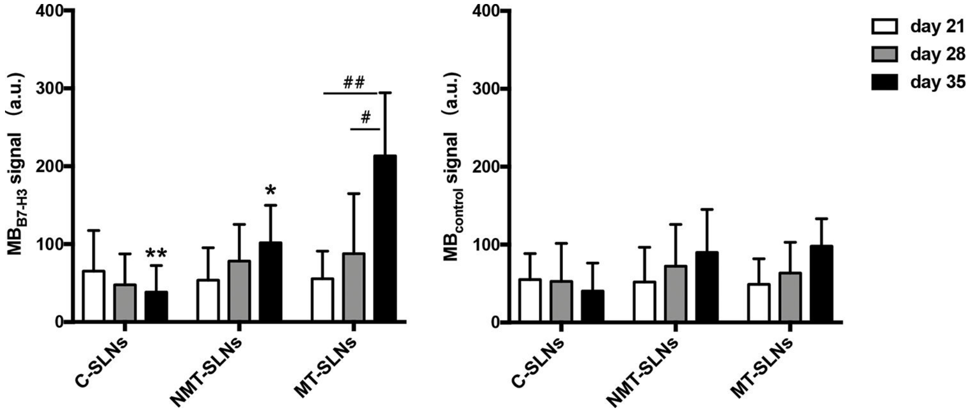

Fig. 3.

Development of $MB_{B7\text{-}H3}$ signal and $MB_{control}$ signal from day 21 to 35. NMT-SLNs and MT-SLNs showed a rising trend in both $MB_{B7\text{-}H3}$ and $MB_{control}$ signal, while C-SLNs showed a declining trend in both of them. MT-SLNs showed a steep increase in $MB_{B7\text{-}H3}$ signal at day 35 as compared to day 28 ($^{\#}$ denotes $P=0.002$) and day 21 ($^{\#\#}$ denotes $P<0.001$). At day 35, MT-SLNs presented significantly higher $MB_{B7\text{-}H3}$ signal than NMT-SLNs (* denotes $P=0.001$) and C-SLNs (** denotes $P<0.001$).

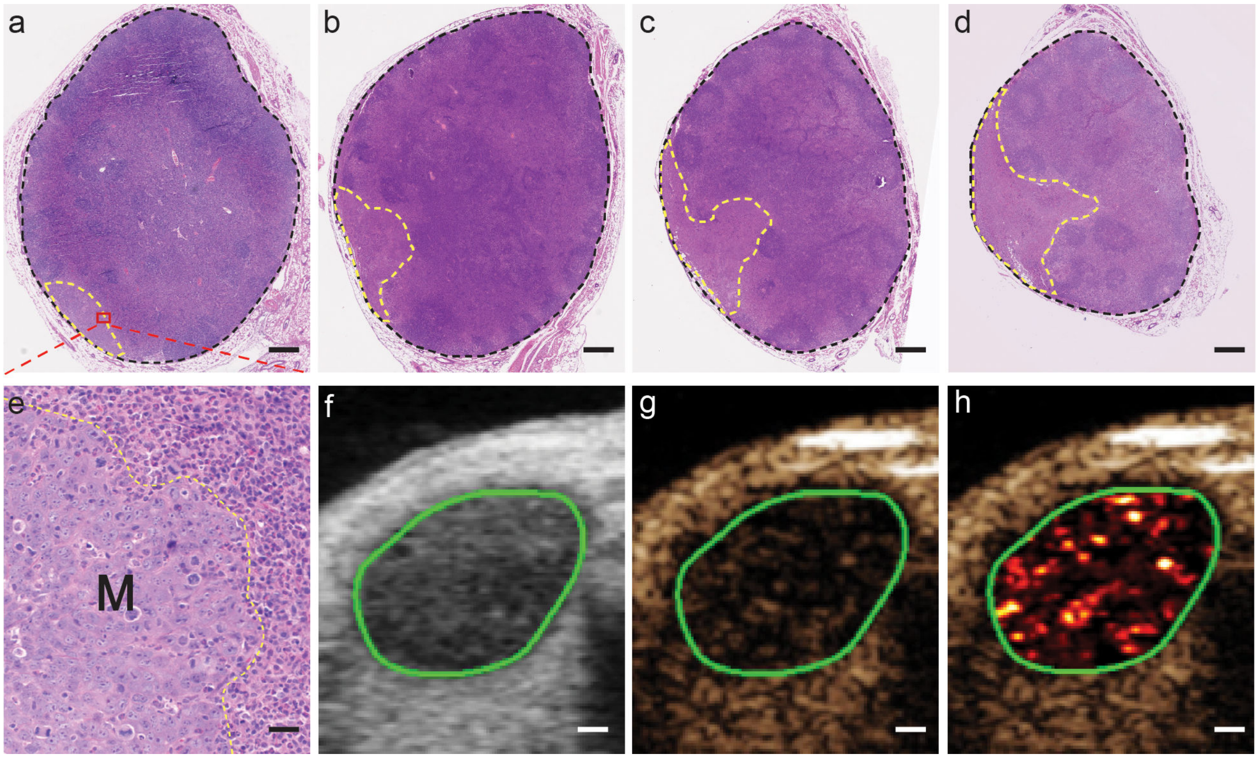

Fig. 4.

MT-SLN with low VFM and corresponding US images. (a-d) Representative H&E-stained sections containing metastases from one MT-SLN. The area of SLN and metastases was calculated over the field of black and yellow dashed border line, respectively. Scare bar=400µm. (e) Zoomed region of the area in the dashed box of fig 4a shows the boundary (yellow dashed line) of metastasis (M) and normal SLN tissue. Scare bar=30µm. B-mode (4f), contrast-mode (4g), and color map images (4h) of the same MT-SLN (VFM: 8%; signal: 48.8). (f-h) Scare bar=600µm.

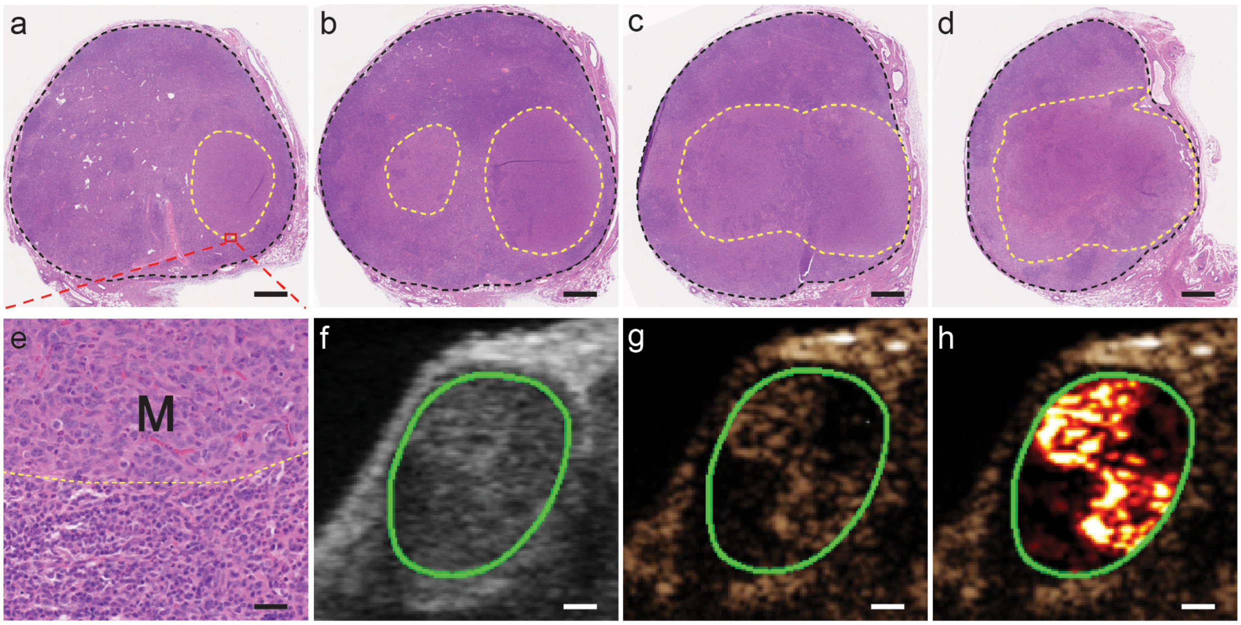

Fig. 5.

MT-SLN with high VFM and corresponding US images. (a-d) Representative H&E-stained sections containing metastases from one MT-SLN. The area of SLN and metastases was calculated over the field of black and yellow dashed border line, respectively. Scare bar=500μm. (e) Zoomed region of the area in the dashed box of fig 4a shows the boundary (yellow dashed line) of metastasis (M) and normal SLN tissue. Scare bar=40μm. B-mode (4f), contrast-mode (4g), and color map images (4h) of the same MT-SLN (VFM: 53%; signal: 245.5). (f-h) Scare bar=700μm.